Monitoring and forecasting hazards from a slow growing lava dome using aerial imagery, tri-stereo Pleiades-1A/B imagery and PDC numerical simulation

Yves Moussallam, Talfan Barnie, Álvaro Amigo, Karim Kelfoun, Felipe Flores, Luis Franco, Carlos Cardona, Loreto Cordova, Virginia Toloza

Monitoring and forecasting hazards from a slow growing lava dome using aerial imagery, tri-stereo Pleiades-1A/B imagery and PDC numerical simulation.

Yves Moussallam[1,2*], Talfan Barnie[3], Álvaro Amigo[4], Karim Kelfoun[2], Felipe Flores[5], Luis Franco[5], Carlos Cardona[5], Loreto Cordova[5], Virginia Toloza[5]

[1] Lamont-Doherty Earth Observatory, Columbia University, New York, USA

[2] Université Clermont Auvergne, CNRS, IRD, OPGC, Laboratoire Magmas et Volcans, F-63000 Clermont-Ferrand, France

[3] Nordic Volcanological Center, Institute of Earth Sciences, Sturlugata 7 – Askja, 101 Reykjavik, Iceland

[4]Servicio Nacional de Geología y Minería (SERNAGEOMIN). Red Nacional de Vigilancia Volcánica, Santiago, Chile

[5]Observatorio Vulcanológico de los Andes del Sur, Servicio Nacional de Geología y Minería, Temuco, 03850, Chile

*Corresponding author: Yves Moussallam; yves.moussallam@ldeo.columbia.edu

Keywords: structure from motion; volcanic dome; photogrammetry; dome collapse; dome growth; pyroclastic flow

ABSTRACT

In December of 2017, a lava dome emerged at the Nevados de Chillan volcanic complex in the southern Andean volcanic zone, Chile, at the base of a summit crater excavated by explosions during two preceding years of unrest. This posed a number of potential hazards to the surrounding touristic region, so the eruption was carefully monitored. Structure from Motion techniques were used to generate DEMs from satellite and aerial images, from which several useful measurements could be made. Dome growth was characterised at an unprecedented resolution, allowing for the calculation of discharge rates and effusion rates in near real time. A simple model fit to the distance between the dome and crater rim predicted relatively accurately the arrival of the dome toe at the crater rim and the onset of dome collapse outside the crater. Simulations of the path and extent that potential pyroclastic density currents (PDC) generated by dome collapse would follow showed that PDC were not directly threatening populated areas. Over its life cycle as of August 2019, the dome growth was punctuated by frequent explosions, averaging around 30 per day, one of which generated a minor 600 m long PDC on 13 to 15 of July 2018. There appears to be a positive correlation between explosion frequency and lava dome growth rate suggesting that both explosive and effusive processes can coexist, operating at different timescales but responding to the same driving force. A positive correlation is apparent between dome growth rate and seismic activity such as the frequency of tremor and long-period earthquakes suggesting that these might be used as proxies to estimate effusion rate. Initial lava dome effusion rates of 1730 ± 110 m^3/day in January 2018 declined to 100 ± 150 m^3/day in June 2019. These growth rates are extremely slow when compared to other lava domes, about 300 to 600 times slower than the lava domes at Mt Unzen (1992) and Mt. St. Helens (1980).

Highlights:

- Ultra-high-resolution DEM and time series of lava dome growth
- Real time forecasting of initiation of dome gravitational instability
- Simulations of PDC from dome collapse show no immediate threat to populated areas
- Simultaneity of explosive and effusive activities, positively correlated
- Strong positive correlation between effusion rate and seismic event frequencies

1. INTRODUCTION

Lava domes form by the slow effusion of typically felsic and viscous magma at the surface and are commonly associated with hazardous phenomena. The most common hazard is the formation of pyroclastic density currents generated by partial or complete collapse of the dome, also termed Merapi-type pyroclastic flows. Examples of these types of flow include the 1991 eruption period at Unzen volcano (e.g., Sato et al., 1992), the 1994 eruption period at Merapi volcano (e.g., Abdurachman et al., 2000), the 1996-97 eruption period at Soufriere Hills volcano (e.g., Cole et al., 1998) and the 1998–99 eruption period at Colima volcano (e.g., Saucedo et al., 2002). Lava domes can also be associated with explosive eruptions and blast generating Peléan-type pyroclastic flows such as in the 1956 eruption at Bezymianny volcano (e.g., Gorshkov, 1959), the 1980 eruption at Mt St. Helens volcano (e.g., Lipman and Mullineaux, 1981), the 1991 eruption period at Unzen volcano (e.g., Sato et al., 1992), the 1997 eruption at Soufriere Hills volcano (e.g., Woods et al., 2002) and the 2010 eruption at Merapi volcano (e.g., Komorowski et al., 2013). Monitoring the growth and behaviour of active lava domes is therefore of primal importance to forecast potential explosive events and mitigate their hazards.

In late December 2017 (exact date unknown), after two years of increased activity with frequent eruptions propelled by the emplacement of a small intrusion of magma at shallow level (Moussallam et al., 2018), lava reached the surface at the Nevados de Chillán volcanic complex forming a small lava dome (Fig. 1). Subsequent growth of the lava dome was monitored by bimonthly helicopter overflights operated by the Observatorio Volcanológico de Los Andes del Sur (OVDAS), part of the Servicio Nacional de Geología y Minería (SERNAGEOMIN). As helicopter flights became unavailable to continue the monitoring, we tasked the monthly acquisition of Pleiades-1 tri-stereo optical imagery. We used aerial

78 photographs taken during observation flights and tri-stereo optical imagery to construct ultra-
79 high-resolution digital elevation models (DEM) of the summit area and precisely measure the
80 dome growth rate and extruded volume over a period of nineteen months. During this period,
81 we used these measurements to forecast the onset and location of rock fall events. Finally, we
82 performed numerical modelling to predict the extent of PDC that would be generated by a
83 potential dome collapse or large explosion in order to assess hazard to nearby population.

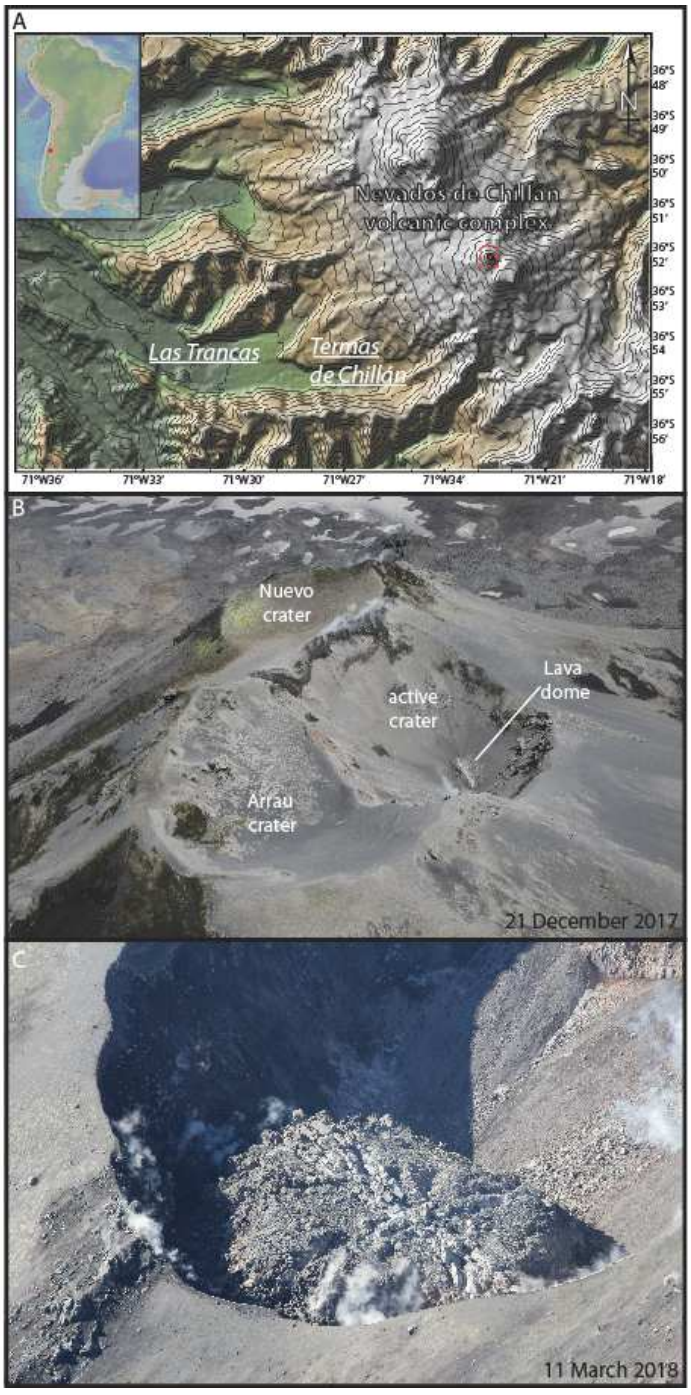

***Figure 1**: **A**: DEM of the Nevados de Chillán Volcanic Complex and surrounding valleys (Global Multi-Resolution Topography grid version 3.8 source: GeoMapApp). The towns of Las Trancas and Termas de Chillán (combined permanent populations of 1600 rising to 30,000 during the tourist season) are shown. Contour lines are drawn every 100 meters and go from 3200 to 600 m. Red circle shows the location of the active crater, red dashed rectangle shows the location of the view shown in (B). **B**: Aerial photograph taken on 21*

December 2017 looking W-NW. The emergence of an ellipsoid-shaped lava dome (35 m long by 22 m wide) with a central fissure can be seen in the centre of the newly formed crater (see Moussallam et al., 2018 for detailed eruption history and formation of the new crater). ***C****: Aerial photograph taken on 11 March 2018 looking south and showing the now 119 m long by 79 m wide lava dome. The central crease structure can be observed with lava flowing away from both directions. Crater's dimensions are 205 by 155 m.*

2. METHODS

In this paper we (i) apply Structure from Motion (SfM) to make measurements of dome volume and geometry from stereo images, (ii) fit Bayesian models to these measurements using Hamiltonian Monte Carlo techniques to estimate effusion rates and predict the start of dome collapse, and (iii) use 2 layer numerical modelling of pyroclastic flows to predict the potential extent of dome collapse. We discuss each of these three techniques in the following sections.

2.1 Digital Elevation Model generation

Aerial photogrammetry

Helicopter flights were performed on 21 December 2017, 09 January 2018, 12 January 2018, 16 January 2018, 23 January 2018, 07 February 2018, 22 February 2018,11 March 2018, 4th April 2018, 18th April 2018, 16 July 2018 and 9th August 2019. Flight height was typically around 3400 to 3700 m altitude and circular flight paths were performed around the summit area in order for aerial photograph to capture the lava dome from all angles (Fig. S1). Cameras were operated manually. Cameras used to take the photograph were equipped with GNSS (GPS of accuracy strictly better than 10m) to provide an approximate position of the camera. 3D models were constructed after each helicopter overflight using the Agisoft Metashape (Agisoft LLC., St. Petersburg, Russia) modelling software (Fig. S1). The Structure

116 from Motion (SfM) software identifies and matches scale invariant features in each images,
117 performs bundle adjustments to refine the camera positions and construct a georeferenced
118 dense point cloud. The georeferenced dense point cloud is then (1) processed with soft-copy
119 triangulation to reconstruct the scene geometry and create a solid 3D mesh (e.g., Burns et al.,
120 2015) and (2) used to construct a DEM. On several occasions however, the internal camera
121 GPS did not work and georeferencing was achieved using easily identifiable features in
122 previously reconstructed DEM as Ground Control Points (GCPs). Pixel resolution on the
123 DEMs varied from 10 cm to 1 m (see supplementary table S1 for details).
124
125 *Tri-stereo satellite optical imagery processing*
126 The PLEIADES constellation consists of two satellites in Low Earth Orbit imaging the Earth
127 at 0.7 m resolution across a 20 km wide swath in the panchromatic band. The satellites are
128 particularly agile, allowing them to acquire multiple images of a target from different angles
129 during a single overpass (Gleyzes et al., 2012). This stereoscopic facility has been extensively
130 used to measure volcanic deposit volumes (e.g. Bagnardi et al., 2016; Di Traglia et al., 2018;
131 Carrara et al., 2019; Ganci et al., 2019a, 2019b). Pleiades images were acquired in tristero
132 mode (three views from one overpass) at roughly monthly intervals from October 2018 to
133 June 2019. Images acquired in February and April 2019 had views of the dome obscured by
134 degassing activity and could not be used to generate DEMs.
135
136 We used the MicMac Structure from Motion software suite (Rupnik et al., 2017) to create the
137 DEMs, following the Pleiades examples in Pierrot-Deseilligny et al., (2014), which we
138 summarise briefly here. First the Rational Polynomial Coefficients (RPCs) which are supplied
139 by the data provider and define the polynomial functions that map 3D geographic space to 2D
140 image space were converted to MicMac format using Convert2GenBundle. Then matching

points are automatically found across all possible pairs of images. This is accomplished using the Tapioca tool in 'All' mode, which uses the Sift+ (Scale Invariant Feature Transform) algorithm (Lowe, 2004) to find tie points. For this step the images were scaled to a width of 10000 (a scaling factor of ~0.5) to save memory. These tie points overdetermine the location and orientation of the imaging systems and so can be used to improve the estimated RPCs using a least squares Levenberg-Marquardt mimization, implemented in the Campari module, improving their accuracy – this is also known as Bundle Block Adjustment. Finally, the DEM is generated from the images using the adjusted RPCs with Ann matching by the Malt tool using the dense matching module UrbanNME.

Vertical precision for both Aerial and Pleiades DEMs were estimated by randomly sampling one hundred points over a stable area (Nuevo crater) and interpolating values at these points for all DEMs, the median height for each sampling point was calculated and subtracted from each height to give a collection of deviations from the median for each point (Fig. S2). The median of all the aerial and Pleiades absolute deviations were then taken, to give the Median Absolute Deviation, or MAD statistic, which came to 1.00 m for Pleiades and 0.476 m for aerial DEMs.

2.2 DEM alignment

The aerial and Pleiades DEMs were found to be misaligned with standard topographic models such as Shuttle Radar Topography Mission (SRTM, Farr et al., 2007), as well as misaligned with each other. We aligned our DEMs using the pc_align tool of the NASA Ames Stereo Pipeline software suite (Shean et al., 2016), using the Similarity-Point-to-Point Iterative Closest Point (ICP) alignment method. This solves for rotation, translation and scaling to align one DEM with another. The area to be used for alignment was selected by masking out

areas where the DEMs showed evidence of change, was noisy, interpolated or otherwise noticeably inaccurate (Fig. S3). For the dome, we then aligned the 21st December 2017 DEM with SRTM, and aligned all subsequent DEMs with the aligned 21st December DEM. This ensured all our DEMs were aligned with each other as well as being at roughly the right geographic location and scale. In early 2019 it became apparent that a gulley was developing below the dome with a depositional fan at the distal end, which could potentially account for some of the erupted volume. We found that DEMs aligned using the area around the dome were poorly aligned around the gulley and fan, and vice versa, so the DEMs were aligned again using an area surrounding the gulley and fan (Fig. S3). Only data from 16th January 2019 onwards reliably and systematically covered the whole feature, so the 16th January 2019 DEM was chosen as our reference and all subsequent DEMs were aligned with that.

2.3 DEM differencing

For the dome, we took the 21st Dec 2017 DEM as our reference surface, above which all volumes are measured. This DEM was then resampled to and subtracted from every other aligned DEM, using the ASP geodiff tool to give a time series of differential DEMs (dDEMs) each with the resolution of the newer DEM. These are effectively thickness maps of the dome at given dates relative to our 21st Dec 2017 reference surface. For the gulley and fan, we took the 16th January 2019 DEM as our reference surface and differenced all successive DEMs with it. Histograms of the dDEMs over stable regions are shown in Fig S4 giving the Median Absolute Deviation (MAD) and standard deviation for each dDEM.

2.4 Volume calculations

Dome volumes were calculated by digitising each dome and integrating the dDEMs over these shapes. We estimated uncertainties in these volumes by moving the plan shapes of each

dome to a neighbouring crater that is well resolved in all the DEMs (Arrau crater, in Figure 1b), but doesn't show any appreciable topographic change, and measuring the volume for all dDEMs. This gives a number of estimates of a 'dome' of zero volume for each dome shape, from which we took the standard deviation as the error. For the gulley and fan a similar procedure was performed where we moved the shape delineating the feature to nearby regions where no significant volume change is expected. We measured the net volume of the gulley and fan to try to estimate the volume of fresh volcanic material present. The hope being that the negative contribution of material removed from the gulley is compensated by the net positive contribution of deposition in the fan. In reality, remobilised material is unlikely to pack back down to the same volume, so it is likely that the values would be an overestimate – we discuss this further in the results section.

2.5 Time Averaged Discharge Rates

Time Averaged Discharge Rates (TADRs) (defined after Harris et al., 2007) were calculated by differencing successive volumes and dividing by the time interval between them. Uncertainties in TADR were found by simple propagation of errors.

2.6 Effusion rates

Effusion rates (or the instantaneous discharge rate) were calculated by fitting a model to the time series of volumes and finding its derivative. In the absence of an obvious physical model to fit to the data we chose a Gaussian Process (or GP), which can be considered a distribution over functions (Görtler et al., 2019); an infinite dimensional multivariate normal distribution where each dimension maps to a point in the domain on which we wish to define a function. We adopt a Bayesian approach to fitting the GP, where we seek to calculate the posterior distribution, $p(\theta \vee d)$, over the parameters θ of our model in light of our data, d:

$$p(\theta|d) = \frac{p(d \vee \theta)p(\theta)}{p(d)}$$

Where $p(d \vee \theta)$ is the likelihood, $p(\theta)$ is the prior distribution over the parameter space and $p(d)$ is effectively a normalising constant that can be ignored. The GP is defined by the kernel function that is used to calculate the covariance matrix of any multinormally distributed subset of variables in the GP, and here we choose the simple squared exponential kernel function:

$$K_{ij} = \alpha^2 exp\left(\frac{-1}{2\rho^2}\left(t_i - t_j\right)^2\right)$$

Where K_{ij} is the ij^{th} element of the covariance matrix K that specifies the covariance between points t_i and t_j, and α and ρ are 'hyperparameters' that specify the variability and length scale of the functions drawn from the GP. Gaussian processes have the property that their derivatives are also GPs and so can be included in the covariance matrix (e.g., Riihimäki and Vehtari, 2010) provided the kernel function is modified appropriately for the ij elements where one or both points are gradients:

$$K'_{ij} = \alpha^2 exp\left(\frac{-1}{2\rho^2}\left(t_i - t_j\right)^2\right)\left(\frac{-1}{\rho^2}\left(t_i - t_j\right)\right)$$

$$K''_{ij} = \alpha^2 exp\left(\frac{-1}{2\rho^2}\left(t_i - t_j\right)^2\right)\frac{1}{\rho^2}\left(1 - \frac{1}{\rho^2}\left(t_i - t_j\right)^2\right)$$

Where K'_{ij} is the ij^{th} element of the covariance matrix where the i^{th} element is a gradient and K''_{ij} is that where both the i^{th} and j^{th} elements are gradients. We thus have a model parameter space with dimensions of θ, α, ρ, V, V'. We use a non centred model (Betancourt and

Girolami, 2013; Papaspiliopoulos et al., 2007) as this is computationally easier and can avoid some problems during Monte Carlo sampling. Briefly, in a non-centered GP model we place an independent and unit-normally distributed prior on our volumes V_i and gradients V_i' at our points t_i and transform them using the Cholesky factor of the covariance matrix. The model was fit to standardised data, and the following priors were selected:

$$p(\alpha)\ normal(0,1)$$

$$p(\rho)\ inv_{gamma}(5,5)$$

$$\eta\ normal(0,1)$$

$$K = k(\alpha, \rho)$$

$$L = Cholesky(K)$$

$$\begin{pmatrix} V \\ V' \end{pmatrix} = L.\eta$$

For the likelihood, we assume our measured volumes are distributed about those predicted by the GP by their observed uncertainties as calculated above in section 2.4:

$$V_{i,obs}\ normal\left(V_i, \sigma_{i,obs}\right)$$

This model was implemented in the Stan probabilistic programming language (Carpenter et al., 2017), which uses Hamiltonian Monte Carlo to draw samples. These samples were then used to calculate expectations over the posterior distribution (or PD) such as the mean and standard deviation at our points of interest t_i, t_j. Additionally, for every sample $V_i$we generate an additional sample $V_i + normal(0, \sigma_i)$ which gives us a draw from the Posterior Predictive Distribution (PPD). One can think of the PD as giving the best estimate of the volumes and effusion rates in light of our priors and data, while PDD gives the measurements we might expect to make given the above, and, additionally, the measurement error.

263

264 **2.6 Predicting the onset of dome collapse**

265 During the first months of extrusive activity, the lava dome was filling and remained
266 contained in a crater formed by the last two years of explosive activity (Moussallam et al.,
267 2018). As long as the dome was contained within this crater there were no external reason for
268 it to become unstable and collapse (i.e. the dome might still become unstable due to internal
269 overpressure but not due to gravity). In April 2018, DEMs produced by aerial
270 photogrammetry and resulting growth rates were used to forecast future dome growth and the
271 time at which the dome was expected to reach the crater rim, hence becoming partially
272 unstable and starting to generate rock falls (Fig. 5). To predict the time at which this was to
273 happen, we developed a simple conceptual model of the dome growth in a geometry
274 constrained by an inverted conical-shaped crater of height H, radius R, volume V and half
275 angle θ (Fig. 5 C). Within the crater, the level of the foot of the dome forms a horizontal
276 surface at height h, of radius r, that forms the top of a smaller inverted cone of volume v. The
277 horizontal distance d between the dome edge and crater rim can be expressed as a function of
278 effusion rate E and time t as:

279 $$d = R - \sqrt[3]{\frac{3Etan(\theta)\,\mathrm{t}}{\pi}}$$

280 Using this relationship, we then fitted the data presented in Fig. 5A using a function of the
281 form:

282 $$d = A - \sqrt[3]{B(t - t_0)}$$

283

284 As before the model was fitted using Stan, as above, although in this instance flat priors were
285 used.

286 **2.7 Computer simulation of dome-collapse and explosion induced PDC**

287 During the extrusive activity, a possible scenario was that as the lava dome growth continued,
288 larger portions of the dome might eventually become gravitationally unstable and partial or
289 complete dome collapse might occur, associated with pyroclastic density currents (PDC). In
290 order to determine the spatial area likely to be affected by potential PDC we used the two-
291 fluids version of the VolcFlow numerical model (Kelfoun, 2017; Kelfoun et al., 2017) that
292 simulates concentrated part of PDC (i.e. the block-and-ash flow), the dilute part (ash-cloud
293 surge) and their interaction. Surge can be formed from the concentrated part and, inversely,
294 can form concentrated parts by sedimentation. For details on the method and on equation
295 used, the reader is referred to Kelfoun (2017).
296
297 We simulated two scenarios; a dome collapse and an explosion. For both scenarios, the total
298 volume of rocks forming the concentrated flow was of 6.4×10^6 m^3 which is the size of the
299 Merapi 2010 Eruption. This size was used as to represent a hypothetical worst-case scenario
300 and is not related to the current dome volume which is an order of magnitude smaller.
301 Although we stress that larger eruptions are of course possible. Concentrated pyroclastic
302 currents were simulated starting from a circular zone of 50 m in radius for the dome collapse
303 scenario, and a zone of 500 m radius for the explosion scenario. These starting locations were
304 used to simulate eruption initiated by dome collapse, hence starting at the current dome
305 location in the first case and eruption from explosion that could happen anywhere within the
306 general summit location in the second case. At the source area, the initial velocity is zero. The
307 concentrated mass then accelerates along the topography forming a surge. Since model results
308 are strongly dependent on the mass rate at the source, two initial durations of genesis were
309 used for each scenario: 60 and 600 seconds. Short durations (i.e., high mass rates) simulations
310 form widespread concentrated flows and powerful surges. Long durations (i.e., low mass
311 rates) simulations form very small surges and flows, channelized in a few drainages valleys

312 and reaching long distances. Fourteen parameters must be defined to run the two-fluids
313 simulation. Some parameters are known (e.g. gravity or topography) or can be estimated from
314 field observations, at least within a given range (e.g. density of the PDCs or volume of the
315 dome that collapse). Five parameters are unknown: three rheological parameters that rule the
316 PDCs dynamics, the exchange coefficient from the concentrated to the dilute PDC, and the
317 density of the mixture formed by the fine particles of the concentrated PDC with volcanic or
318 atmospheric gases. These parameters have been estimated by reproducing real emplacements
319 of the 2010 PDCs at Merapi volcano and the 1997 PDCs at Montserrat, and are similar for
320 both fields cases (Kelfoun et al., 2017; Gueugneau et al., 2019). For the present study, we
321 have chosen to use the parameters of the 2010 eruptions of Merapi volcano.
322

323 ## 3. RESULTS

324 The time series of aerial and Pleiades DEMs show the growth of the dome from a small
325 mound at the base of the summit crater in December 2017 to overflowing sometime between
326 April and July 2018 (Fig. 2). Cross sections across the DEMs show the dome maintained a
327 relatively flat surface, consistent with an extruding fluid with a finite yield strength (Fig. 5B),
328 until explosions from January 2019 onwards began to excavate a crater on the top of the
329 dome. Once the dome reached the rim of its host crater, a combination of rock falls and
330 pyroclastic flows appears to have cut a gulley into the volcano's northern flank, which is
331 terminated by a depositional fan. These features are visible as negative and positive height
332 changes in the dDEMs in Fig. 3., respectively. Cross sections of the gulley and fan in the
333 DEMs reveal the progressive incision of the former and growth of the latter from March to
334 June 2019. However, it should be noted that snow is present on the lower flanks of the
335 volcano, so changes in elevation may also partially be a function of changes in snow
336 thickness.

337

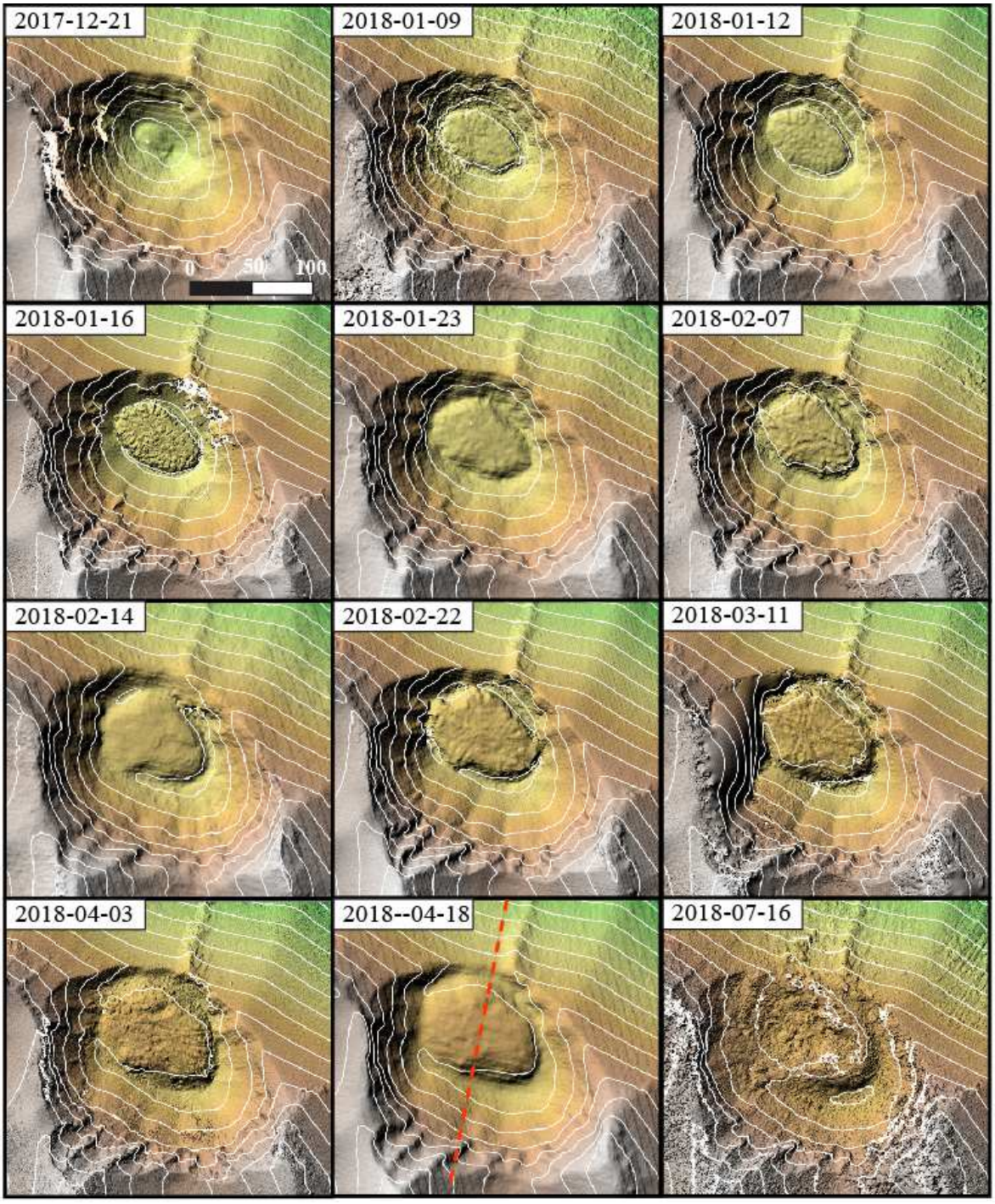

338

339 ***Figure 2*** *(panel 1 of 2): DEMs of the summit area after helicopter observation flights and*
340 *Pleiades 1 tri-stereo imaging showing the growth of the lava dome in the active crater. Red*
341 *dash line shows the location of the profile in Fig. 5B. Reconstruction of the area on the west*
342 *side of the dome on 11 March 2018 is inaccurate due to obstruction by gases during*
343 *observation flight, so is the area from the center to the SE of the dome on 08 December 2018.*

344 *Contour lines are drawn every ten meters. Contains information © CNES (2018-2019) and*

345 *Airbus DS (2018-2019), all rights reserved, commercial use prohibited.*

346

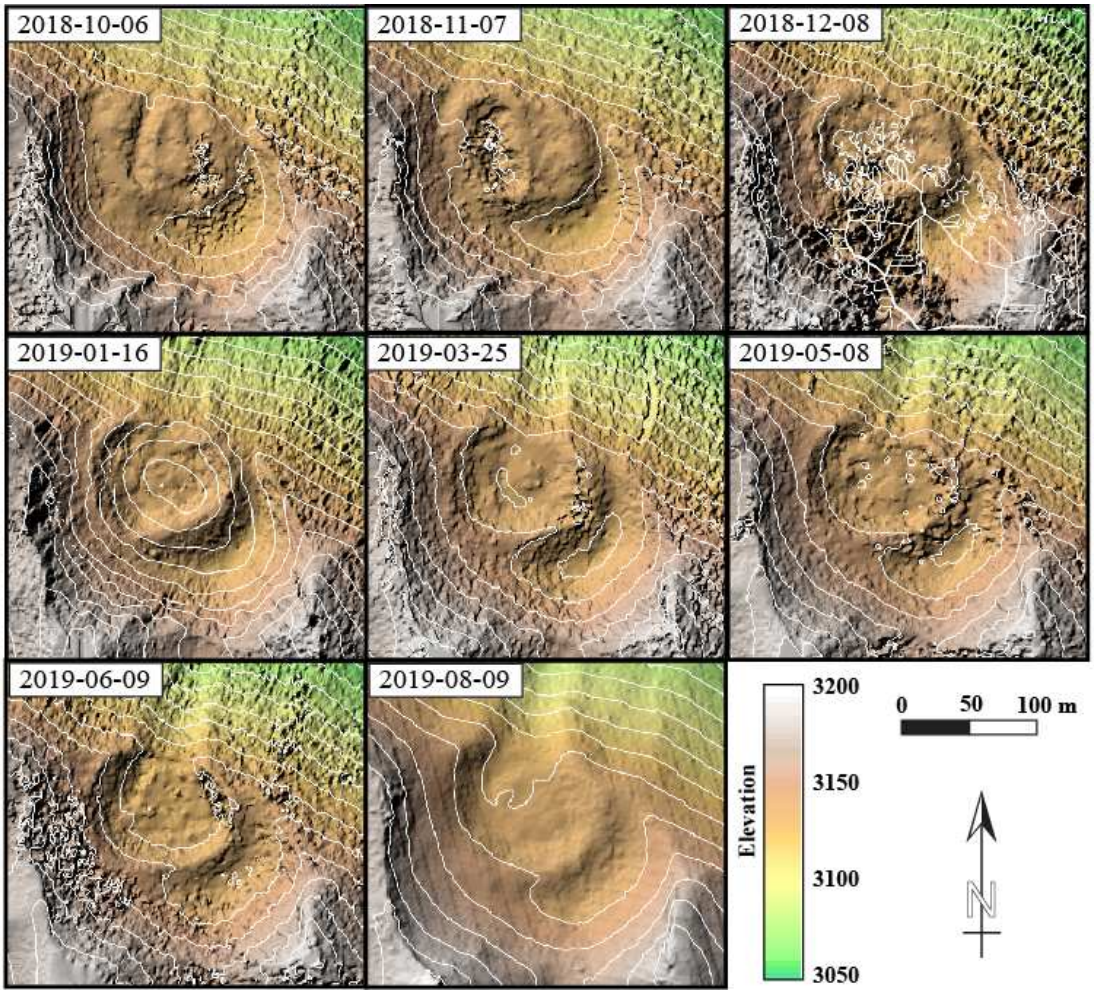

347

348 ***Figure 2*** *cont (panel 2 of 2)*

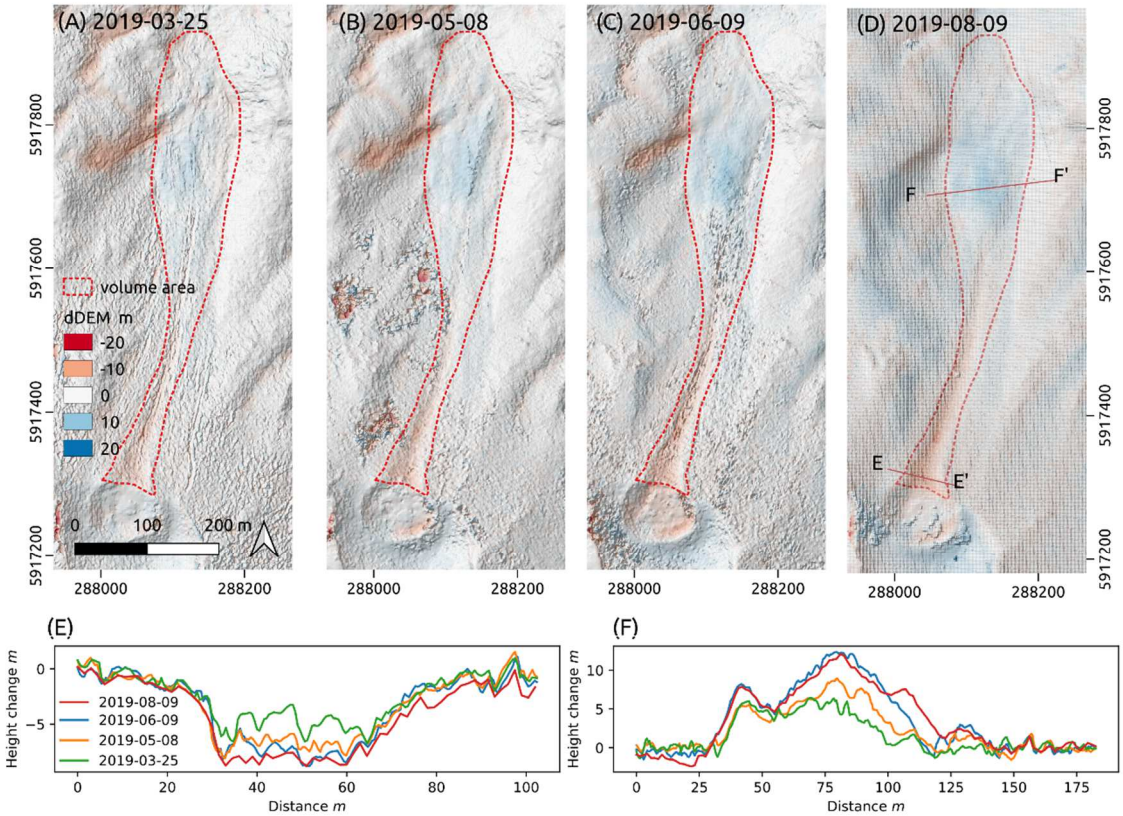

***Figure 3**: Development of the gulley and fan in 2019. (A)-(D) Hillshade of Pleiades DEMs overlain on dDEM with datum taken as the 2019-01-16 dem for 2019-03-25, 2019-05-08, 2019-06-09 and 2019-08-09 respectively. Red colors indicate erosion, blue deposition. Dashed red polygon shows integration area for volume calculations. Cross sections E-E' across the gulley just below the dome and F-F' across the depositional fan are shown in figures (E) and (F). Note the continuous erosion of the gulley in (E) and growth of the fan in (F) across the period. Contains information © CNES (2018-2019) and Airbus DS (2018-2019), all rights reserved, commercial use prohibited.*

Dome volumes and their uncertainties are given in Table 1 and shown in Fig. 4. We were able to estimate dome volumes with uncertainties of approximately 4% and 3% for Aerial and Pleiades DEMs, respectively. The dome grew steadily, reaching a maximum of 3.97e5m^3 in August of 2019. A small decrease between May and June 2019 is presumably due to increasing collapses and explosions. These volumes gave Time Averaged Discharge Rates (TADR) values that fluctuate quite substantially, varying between 1.17e3 and 2.39 e3 m^3day^{-1} in the first 3 months, before declining over the rest of the observation period. Uncertainties in TADR averaged 33% for Aerial dDEMs and 121% for Pleiades dDEMs, although the high latter value is largely a function of low effusion rates during the Pleiades acquisition period. By fitting the GP model we were able to estimate the instantaneous effusion rate, which was found to be 1.73e3 m^3 day^{-1}on the 9th January of 2018 before declining to around ~ 1e3 m^3 day^{-1} and remaining roughly constant from early May to July 2018 before declining again more rapidly in mid-2019. Effusion rate estimates using the GP model had uncertainties of between 3% and 422%.

Seismic activity also shows a remarkably similar pattern to the dome effusion rate during the observation period (Fig. 4D). The total number of seismic event decreases sharply during the first three to four months before reaching a plateau with fairly constant activity from April 2018 to January 2019, followed by another period of decreasing activity from January 2019 to June 2019 and increasing again in July to August 2019. The number of explosions at the crater per day (Fig. 4C) also follows the same temporal evolution, averaging 60 to 40 explosions per day in the first three months before stabilising around 35 explosions per day from April 2018 to April 2019, dropping below 20 eruptions per day in June 2019 before increasing sharply in July-August 2019. A direct comparison between our modelled mean monthly effusion rate and measured mean monthly numbers of seismic events is shown in

Fig. 5. The positive correlation between the modelled effusion rate and the frequency of long-period earthquakes, explosions and tremors is apparent (with R^2 of 0.9, 0.7 and 0.5 and P-values of 10^{-10}, 10^{-6} and 10^{-4} respectively). Looking in more details at Fig. 5, three different regimes seem to emerge. The first is for effusion rates below ~100 m^3/day, the number of seismic events (long-period earthquakes, explosions, and tremors) is high in comparison with the effusion rate and increases quickly with increasing effusion rate. The second regime, for effusion rates between ~100 and ~900 m^3/day shows no correlation between effusion rate and seismic activity with the number of long-period earthquakes, explosions and tremors remaining fairly constant over this large range of effusion rates. The third regime, for effusion rates between ~900 and ~1700 m^3/day shows again a strong positive correlation between effusion rates and numbers of explosions, tremors, and long-period earthquakes but with an increase in seismic event with increasing effusion rate that is slower from the correlation observed in the first regime.

The net volume of the gulley and fan (volume accumulated in the fan minus volume eroded in the gulley) grew to 5.24e4 m^3 from January to June 2019, and then fell slightly to 4.0e4 m^3 by August, although errors are high and this may simply indicate that rockfalls had ceased. As the integration area was constant, the error in the volume was also constant at 1.20e4 m^3, however the estimate of the uncertainty is only based on the standard deviation of four 'zero volume' gulley and fan dDEMs, so is itself likely quite uncertain. We measured the net volume of the gulley and fan in the hope that the erosion and deposition of older material cancels out leaving the net contribution of fresh volcanic material, however it seems likely that redeposited older material will not compact back down, and so there will be a net positive volume even before new volcanic material comes into consideration. The uncertain contribution of snow to these volumes also makes them suspect. However we include them to

show that, in principle, the gulley and fan have a net positive volume that could account for a substantial part of the apparent decline in dome growth in June 2019 - i.e., rather than continuing to contribute to dome growth, it is at plausible that extrusion of further material triggered collapse and diverted material out of the crater instead during this period.

412 ***Table 1**: Volume, Time Averaged Discharge Rates and Effusion Rates for the dome and gulley DEM timeseries. The uncertainties for a given*
413 *value are given to the last two significant figures using concise notation (i.e. 5.04(13)e+04 = 5.04e4 ± 0.13e4). TADR values are given for the*
414 *date at the end of the interval they are measured over. Effusion rates are instantaneous discharge rates predicted by the GP model for the*
415 *specified date. The DEMs used as datums for estimating volumes of the dome and gulley are tinted red and green respectively.*
416

Date	*Type*	*Volume m^3*	*TADR m^3day^{-1}*	*Effusion Rate m^3day^{-1}*	*Gulley volume m^1*	*Gulley TADR m^3day^{-1}*
2017-12-21	Aerial	0.0(1.0)e+03	-	-	-	-
2018-01-09	Aerial	2.49(17)e+04	1.31(10)e+03	1.73(11)e+03	-	-
2018-01-12	Aerial	2.98(18)e+04	1.61(82)e+03	1.72(10)e+03	-	-
2018-01-16	Aerial	3.57(19)e+04	1.48(64)e+03	1.694(88)e+03	-	-
2018-01-23	Aerial	5.04(23)e+04	2.11(43)e+03	1.652(71)e+03	-	-
2018-02-07	Aerial	6.86(27)e+04	1.21(24)e+03	1.552(44)e+03	-	-

2018-02-14	Aerial	8.53(29)e+04	2.39(57)e+03	1.502(38)e+03	-	-
2018-02-22	Aerial	9.79(31)e+04	1.58(54)e+03	1.444(37)e+03	-	-
2018-03-11	Aerial	1.179(34)e+05	1.17(27)e+03	1.319(49)e+03	-	-
2018-04-03	Aerial	1.443(39)e+05	1.15(22)e+03	1.164(71)e+03	-	-
2018-04-18	Aerial	1.540(40)e+05	6.5(3.7)e+02	1.079(77)e+03	-	-
2018-07-16	Aerial	2.419(62)e+05	9.88(83)e+02	8.52(76)e+02	-	-
2018-10-06	Pleiades	3.12(10)e+05	8.6(1.5)e+02	7.14(89)e+02	-	-
2018-11-07	Pleiades	3.240(79)e+05	3.6(4.0)e+02	6.15(97)e+02	-	-
2018-12-08	Pleiades	3.415(92)e+05	5.6(3.9)e+02	5.0(1.0)e+02	-	-
2019-01-16	Pleiades	3.62(14)e+05	5.2(4.3)e+02	3.6(1.0)e+02	0.00(0)e+00	-
2019-03-25	Pleiades	3.77(14)e+05	2.2(2.9)e+02	1.6(1.1)e+02	0.2(1.2)e+04	0.3(1.8)e+02

2019-05-08	Pleiades	3.85(16)e+05	1.8(4.8)e+02	1.1(1.3)e+02	2.0(1.2)e+04	4.1(3.8)e+02
2019-06-09	Pleiades	3.72(15)e+05	-4.0(6.8)e+02	1.0(1.5)e+02	5.2(1.2)e+04	1.01(53)e+03
2019-08-09	Aerial	3.97(14)e+05	4.1(3.4)e+02	0.8(3.5)e+02	4.0(1.2)e+04	-2.0(2.8)e+02

417

418

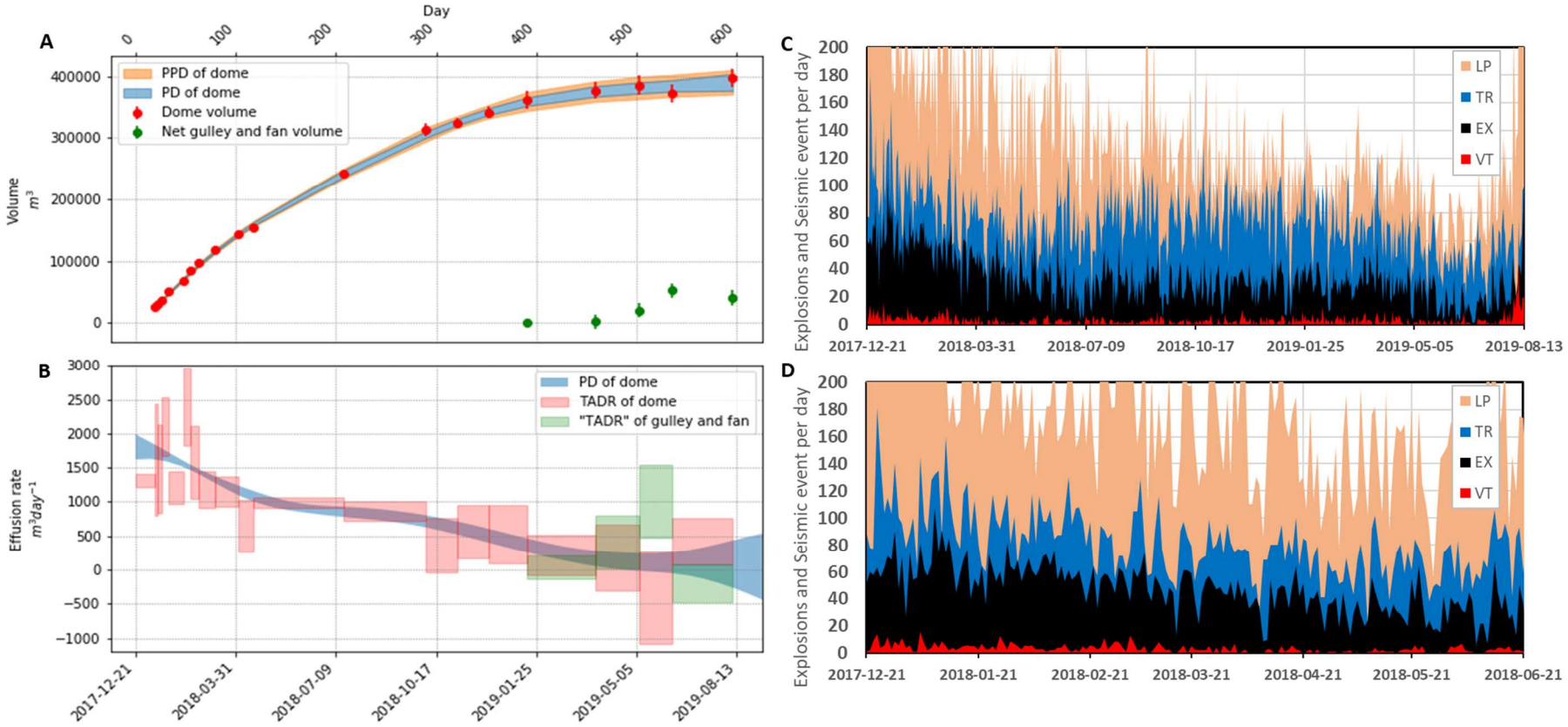

***Figure 4**: **A**. growth of dome and gulley-and-fan; red points are dome volumes, green points net volume of gulley and fan, blue tint is posterior distribution over modelled volume (PD) at ± 1σ, orange tint is posterior predictive distribution of volume measurements (i.e. incorporating measurement error). **B**. Time Averaged Discharge Rates of dome and gulley-and-fan, as well as modelled dome effusion rate. Width of boxes shows duration of averaging interval and height uncertainty for TADR estimates for dome and gulley-and-fan (red and green, respectively). Blue tint shows posterior distribution of modelled effusion rates. **C**. Number of explosions (EX), volcano-tectonic (VT), tremor (TR) and long-period*

425 *(LP) seismic events per day recorded by SERNAGEOMIN's seismic network at Nevados de Chillan. Note the broad correspondence between the*
426 *decreasing lava dome effusion rate and total number of seismic events. The increase in seismic event in August 2019 is due to a new extrusion*
427 *phase not discussed here.* ***D****. Close up of (C) for the first six months of observations showing the close correspondence between number of*
428 *explosions per day and number of seismic events.*

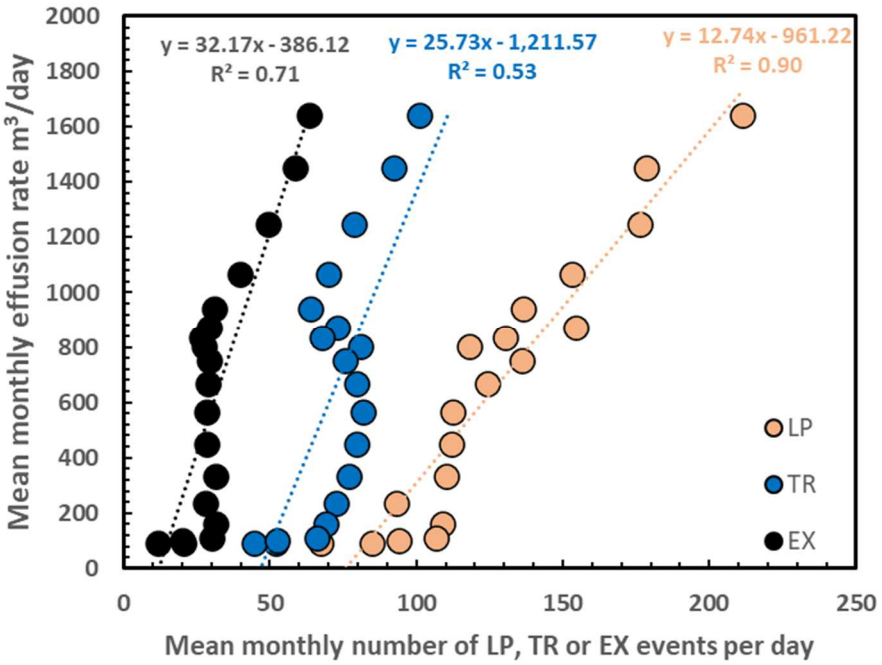

***Figure 5**: Mean monthly modelled effusion rate at Nevados de Chillan for the period of January 2018 to July 2019 compared to the measured mean monthly number of explosions (EX), tremor (TR) and long-period (LP) seismic events per day recorded by SERNAGEOMIN's seismic network. Lava effusion rate appears to be positively correlated with all three types of seismic event but most strongly with long-period earthquakes. In detail three different regime seem to emerge for effusion rates below ~100 m^3/day, between ~100 and ~900 m^3/day and between ~900 and ~1700 m^3/day.*

The predicted time that the foot of the dome would reach the rim is shown on Fig. 7 with the PD and PPD indicating that the dome edge should reach the crater rim sometime in May 2018. Near-real time estimates of the probability of the dome reaching the rim by a given date were produced in April 2018 and updated after each DEM reconstructions. Probability estimates were produced by conditioning on the distance to the rim being equal to zero, and integrating across time, as shown by the curves. This indicated that the dome was likely to have reached the rim by the end of May 2018. Indeed, OVDAS/SERNAGEOMIN cameras

445 then observed the dome at the crater rim on 28 May 2018. No rock fall occurred subsequently
446 until three large explosions on 13 to 15 July 2018 partially destroyed the dome leaving a small
447 crater within the dome and small pyroclastic flows deposits extending 600 m from the vent.
448
449 The results of the pyroclastic flow simulations using VolcFlow are shown in Fig. 8. The maps
450 show the compilation of 10 simulations and indicate the areas that have been affected by at
451 least one simulation. Given the dome location at the time of the calculations (April 2018), our
452 simulations show that PDC generated by dome collapse will always flow towards the north,
453 north-east, away from any populated areas (Fig. 8). In the case of explosions, our simulations
454 suggest that PDC could travel towards the town of Thermas de Chillan, potentially just
455 entering the upper part of the town. The relatively 'flat' topography of the volcano will cause
456 any PDC to disperse and lose velocity rapidly, limiting their extent from the source. By
457 comparison, similar simulation performed on Merapi volcano would results in PDC travelling
458 up to 20 km away from the source while at Nevados de Chillán, this simulation results in PDC
459 confined within 5 km of the vent.

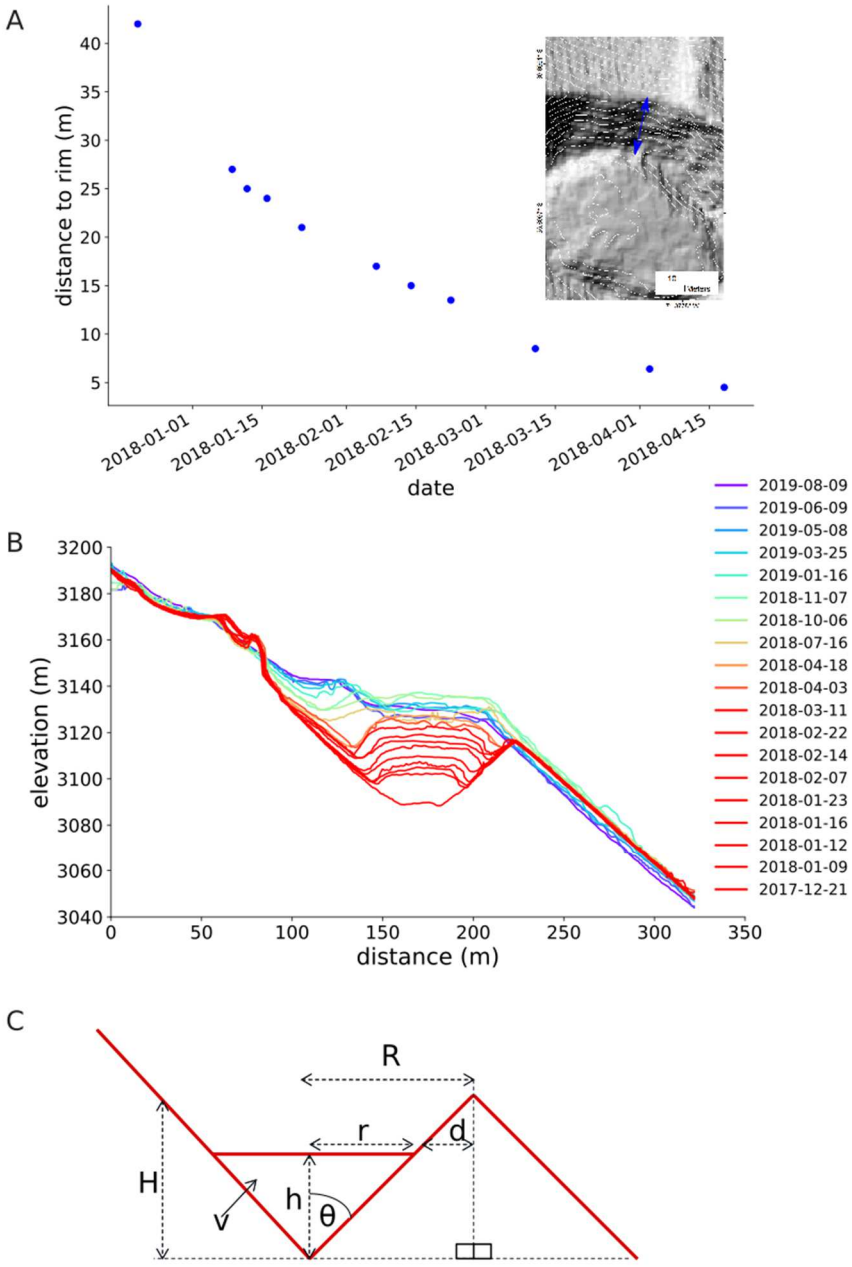

460

461 ***Figure 6**: **A**: Time evolution of the minimum horizontal distance between the foot of the lava*
462 *dome and the lowest point of the crater rim. Inset show a close up of the 11 March 2018 hill*
463 *shaded DEM with one-meter elevation contour lines. The blue arrow shows the remaining*
464 *distance between the lava dome edge and the lowest point of the crater rim. **B**: Cross section*
465 *of dome growth through time (21 December 2017 to 9 August 2019). Location of the profile is*
466 *shown in Fig. 2 (red line). **C**: Simplified conceptual representation of lava dome growth in a*

geometry constrained by a conical-shaped crater and used to model the time evolution of the distance between the dome and crater edge (Fig. 7).

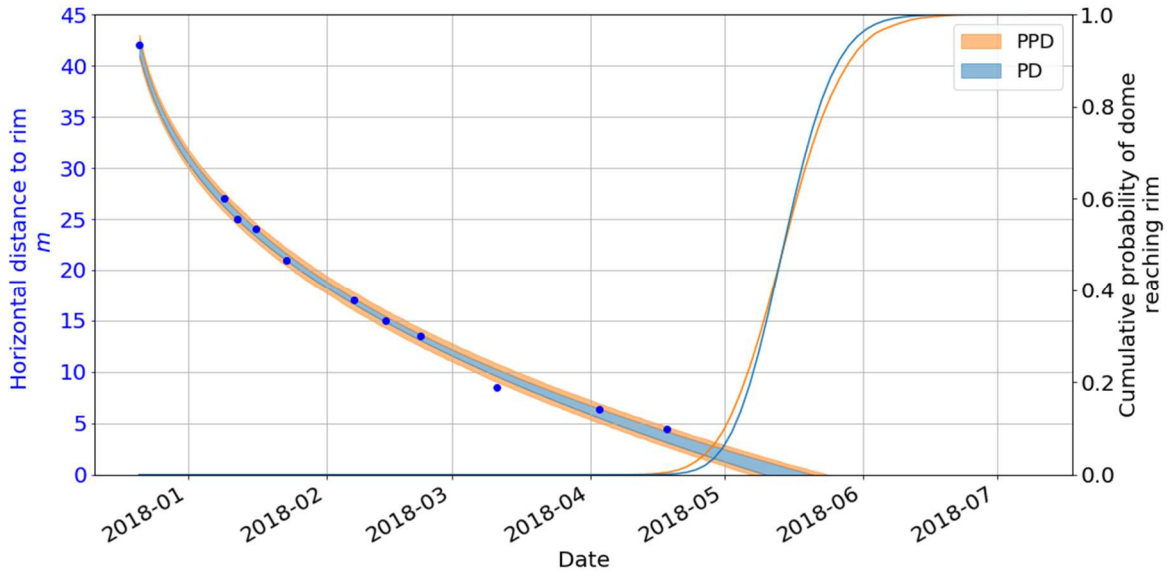

***Figure 7**: Time evolution of the minimum horizontal distance between the foot of the lava dome and the lowest point of the crater rim. Blue tint shows the posterior distribution of modelled distance to rim (PD), while orange tint shows posterior predictive distribution of measured distance to rim (i.e. inclusive of measurement error), both at ± 1σ. Blue and orange curves show the PD and PPD of the cumulative probability distributions of the dome having reached the rim by a given date (i.e. the cumulative distribution of the PD and PDD of the tinted areas conditioned on the distance equalling zero).*

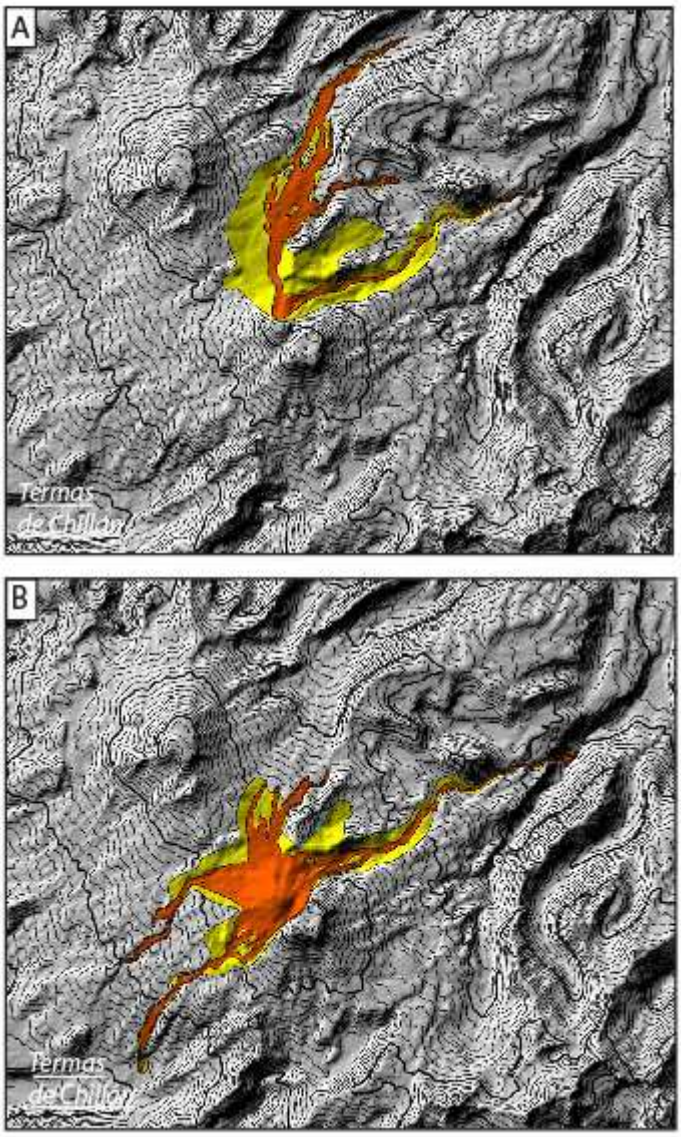

479

480 ***Figure 8****: DEM showing the results of numerical simulations of PDC generated by (**A**) Dome*
481 *collapse and (**B**) Explosion. Area in orange shows the extent of the concentrated fraction of*
482 *the PDC (i.e. the block-and-ash flow), area in yellow shows the extent of the dilute fraction*
483 *(ash-cloud surge). Each map is the results of 10 simulations considering both short (60 s) and*
484 *long (600 s) durations of genesis (i.e., high and low mass rates respectively).*

485

4. DISCUSSION

TADR is a primordial parameter to monitor the evolution of effusive eruptions and yet is not always an easy parameter to determine with sufficient accuracy, precision, or temporal resolution. TADR estimation combined with prior knowledge of a volcano allows hazard assessments based on semi-quantitative event trees (Newhall and Pallister, 2015; Ogburn et al., 2015). Eruption parameters such as extrusion rate and magma composition integrated with (1) a correct statistical analysis of global dome growth episodes database (Newhall and Melson, 1983; Ogburn and Calder, 2012); (2) the recent eruptive record and geological background of the volcano; (3) an adequate interpretation of instrumental and remote sensing monitoring and surface activity; and (4) the use of numerical simulation for modelling volcanic processes, allows for a trusted hazard assessment to be reached in complex risk scenarios situations and these were the parameters used by SERNAGEOMIN's frequent reports on the volcanic activity to forecast future possible scenarios (http://sitiohistorico.sernageomin.cl/volcan.php?iId=32). At Nevados de Chillán the complexity stems from the fact that several touristic facilities are exposed to volcanic risks, the high seasonal population is unfamiliar with volcanic hazards, few roads are available in case of evacuation and the eruption period is very long-lived (started in December 2015).

The rate of dome growth at Nevados de Chillán is one of the lowest ever reported. Table 2 shows the average growth rate at other well studied lava domes. By comparison, the maximum growth rate at Nevados de Chillán of ~1500 m^3/day is about two orders of magnitude slower than most. Comparison with the global dome growth episodes database of Ogburn (2012), reveals that only 12 out of 96 events (12,5%) with calculated time average extrusion rate have comparable values for TADR (<0.1 m^3/s). Nevertheless, comparing with historical eruption at Nevados de Chillán, at the same subcomplex, the current eruptive cycle

511 exhibits similar TADR with the last two historical magmatic eruption. The 2008 Sebastian
512 lava flow, a viscous and dacitic lava flow erupted over an 8 month period with a mean TADR
513 of 0.075 m^3/s and no associated explosive activity (Coppola et al., 2016) and the 1976-1986
514 Arrau eruption with a mean TADR of 0.005 m^3/s (Naranjo et al., 1994). As seen from the data
515 in Table 2, there are no correlations between the growth rates and final dome volumes, so the
516 lava dome growth rates are not informative of the final dome volumes. The time evolution of
517 the dome growth rate observed at Nevados de Chillán is broadly similar to the one observed at
518 other volcanoes. During the 2004 – 2005 eruption of Mount St. Helens for instance the dome
519 growth rate dropped from about 9 to 3 m^3/s within the first three months (Schilling et al.,
520 2008). Similar patterns where observed in the growth rates of the 2009 (Diefenbach et al.,
521 2013) and 1989–1990 (Miller, 1994) lava domes at Redoubt volcanoes, 1991 lava dome at
522 Unzen (Kaneko et al., 2002; Nakada et al., 1995) and 1980 lava dome at Mount St. Helens
523 (Fink et al., 1990; Swanson and Holcomb, 1990).
524
525 The 2017-2019 eruptive episode at Nevados de Chillán is a striking example of effusive and
526 explosive activities taking place simultaneous at a silicic volcano. The inception of dome
527 formation and growth at the surface was accompanied by a sharp increase in explosive
528 activity, averaging less than 5 to 10 eruptions per day prior to December 2017 to reach more
529 than a hundred explosions in a day on 09 January 2018. Eruption of silicic volcanoes
530 commonly show transitions from episodes of explosive activity to regimes of dome formation
531 and vice versa (e.g., Fink, 1987; Nguyen et al., 2014). The transition from one style of activity
532 to the other is thought to occur due to changes in magma ascent rate (e.g., Dingwell, 1996;
533 Martel and Iacono-Marziano, 2015; Woods and Koyaguchi, 1994) or gas loss through
534 permeable conduit walls (e.g., Eichelberger et al., 1986; Jaupart and Allègre, 1991). Neither
535 of these processes however easily explains how concurrent effusive and explosive activity can

be taking place at a single vent. We envision that the conduit at Nevados de Chillán must be filled by a magma penetrated by an extensive fracture network allowing overpressure to be periodically released by ash venting or explosions accompanying magma ascent and dome growth at the surface (Fig. 9). Both processes are operating at different timescales but appear to be strongly positively correlated; periods of heightened explosion frequency corresponding to the periods of heightened dome growth rate and vice versa.

The strong first-order positive correlation between effusion rate and the frequency of explosions, long-period earthquakes and tremors (Fig. 5) suggests (1) that these metrics all tract the same physical process, presumably reflecting variations in overpressure of the magmatic system and (2) that one metric may be used to estimate another. As shown in this study and previous ones, measuring lava effusion rate in real time is not an easy endeavour for any volcano observatory. The strong correlation observed especially with the frequency of long-period events (R^2=0.9) suggests that LP event frequency might be used as a simple way of estimating effusion rate in real time as the eruption continues. A similar observation was made after the 2018 Kīlauea eruption were a positive correlation (R^2=0.6) between effusion rate and real-time seismic amplitude was observed (Patrick et al., 2019). In details however, the relationship between effusion rate and seismic activity at Nevados de Chillán is not a simple and continuous one and three regime can be distinguished showing strong increase in seismic events with increasing effusion rate at low effusion rates (≤ 100 m^3/day), no noticeable changes in seismic activity for effusion rates between ~100 and ~900 m^3/day, and again an increase in the number of seismic events with effusion rate at higher effusion rates (~900 to ~1700 m^3/day) but with a different slope from the first regime (Fig. 5). Following the observation period reported in this manuscript the effusion rate increased again with a lava flow originating from the lava dome flowing down the northern flank. Then again, a strong

positive correlation between effusion rate and the number of explosions, tremors and long-period events was noticed but again with a different slope. The question we are left with is what physical process are these different regimes a reflection of? Regime 3, with effusion rates between ~900 to ~1700 m^3/day, corresponds to the initiation of dome growth and includes the months from January to May 2018 (Fig. 4), regime 2 with effusion rates between ~100 to ~900 m^3/day correspond to the period from June 2018 to April 2019 when effusion rate was decreasing very slowly (Fig. 4) with seismic activity remaining constant while regime 1 corresponds to the months of May 2019 to July 2019 when the effusion rate decreased faster and the number seismic events also dropped (Fig. 4). As the eruption continues and variations in effusion rates are recorded, we will be able to determine if these regimes are replicated or if a strong hysteresis emerges.

The disconnect in terms of ascent processes between the gas phase (sporadically escaping via a fracture network) and the magma might partly explain the extremely slow dome growth rate, much of the overpressure being accommodated by the gas escape leaving little driving force for the magma to ascend. Assuming a conduit radius of 5 meters, our dome growth rates can be translated to ascent rate at the top of the conduit (base of the dome) ranging from 20 meters per day in early 2018 to 9 meters per day in June 2019 (corresponding to decompression rates in the order of 10e-6 Mpa/s). Considering a smaller conduit would lead to higher ascent rate estimates (up to ~130 m/day for a 2 m radius conduit) which would remain much slower than most other well studied volcanic eruptions (see Fig. 9 in Shea, 2017, Fig. 5 in Cassidy et al., 2018 and Fig. 13 in Moussallam et al., 2019 for compilations of ascent rates estimates).

Historical activity records at Nevados de Chillán include eruptive cycles with durations of years to decade (Naranjo et al., 1994). This long-lived eruptive behaviour has been seen at

other volcanoes with lava dome eruption such as Popocatépetl (Mendoza-Rosas et al., 2017) (also see global compilation by Wolpert et al., 2016). In addition, Holocene activity at Volcán Viejo (Las Termas Subcomplex) includes Vulcanian and sub Plinian episodes with 4 fall pumice and at least 3 pyroclastic density currents deposits recognized (Dixon et al., 1999). The wide range of past eruptive styles at Nevados de Chillan hence suggest that our two "worst-case" scenarios modelled here to map the maximum extent of PDC are realistic scenarios. The ongoing mostly effusive eruption could be but a stage in a bigger cycle, with much more explosive events remaining a future possibility. Monitoring the TADR and seismic activity at Nevados de Chillán in near-real time hence remain a priority to forecast and prepare for future activity. Further petrological studies would also help in this endeavour.

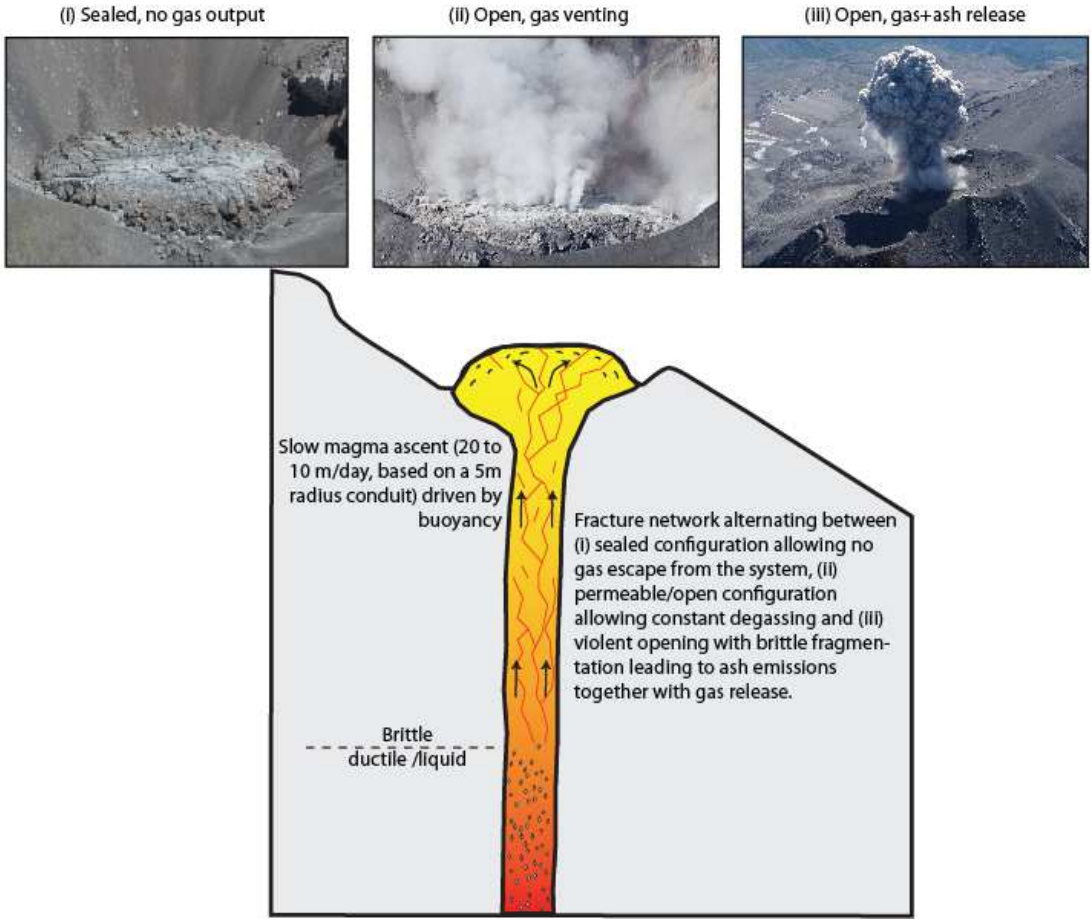

598 ***Figure 9****: Schematic depiction of the magmatic conduit at Nevados de Chillán, perforated by*
599 *an extensive fracture network allowing the release of overpressure through frequent gas-*
600 *venting and explosions. Upper photographs illustrating these three configurations observed*
601 *at Nevados de Chillán. Note that explosion frequency and magma ascent rate seem to be*
602 *positively correlated suggesting that the two processes respond to the same driving forces yet*
603 *operating at different timescale. Gas escape through the fracture network might*
604 *accommodates a large part of the system overpressure, leaving the magma to rise extremely*
605 *slowly.*
606

607 ***Table 2**: Growth rates of lava domes, data are from the compilation of Yokoyama (2005) with*
608 *additional data from *Miller, (1994), **Diefenbach et al., (2013), and ***Schilling et al.,*
609 *(2008).*

Volcano	*Year*	*Final lava dome volume ($x10^7 m^3$)*	*Average growth rate (m^3/day)*
Soufrière St. Vincent	1979	3.5	5.37E+05
Colima	1998	0.04	3.80E+05
Lamington	1951	6	1.58E+06
Redoubt	1987	6.8	2.00E+05
*Redoubt**	1989-1990	8.8	5.01E+05
*Redoubt***	2009	7.2	7.94E+05
Soufrière Hills	1996	6.8	2.00E+05
Turumai	1909	1.5	3.80E+06
Bezymianny	1956	4.2	1.41E+06
Shiveluch	1980	1	1.86E+05
Pelée	1902	3.7	3.16E+05
Mt. St. Helens	1980	1	8.32E+05
*Mt. St. Helens****	2004-2005	7.3	1.58E+05
Santiaguito	1922	20	1.58E+05
Popocatépetl	1996	1.1	1.82E+05
Unzen	1992	5	5.01E+05
Usu	1944	4.4	1.12E+05
Novarupta	1912	0.5	2.51E+04

610

611 **5. CONCLUSIONS**

612 We have used aerial photogrammetry and Pleiades-1 tri-stereo imagery to produce ultra-high-
613 resolution DEMs tracking the growth of a lava dome at the Nevados de Chillán volcanic
614 complex. We found that (i) The dome growth started as fairly stable over the first three
615 months before decreasing over time (ii) The growth rate is orders of magnitude slower than
616 most other lava domes (iii) Prediction of the time at which the lava dome should reach the
617 crater rim proved accurate (iv) Modelling of dome-collapse-generated PDC showed no direct
618 threat to populated areas but PDC generated by large explosions could travel towards
619 populated area (v) The coexistence and simultaneity of effusive and explosive activity is
620 uncommon and may contribute to explains the resulting exceptionally slow ascent rate (vi)
621 Positive correlation between dome growth rate, eruption frequency and seismic activity
622 suggest that they all respond to the same driving force and that the frequency of LP event
623 could be used as a proxy of effusion rate for operational monitoring.
624

ACKNOWLEDGEMENTS

Pleiades images were acquired as part of the CNES' ISIS scientific support program (proposal ID: 2018-012-Sci, PI: YM), © CNES (2018-2019) and Airbus DS (2018-2019), all rights reserved, commercial use prohibited. This work was supported by public funds received in the framework of DINAMIS-GEOSUD, a project (ANR-10-EQPX-20) of the program "Investissements d'Avenir" managed by the French National Research Agency. We are very gratefully to two anonymous reviewers for their constructive comments and to Jean-Philippe Avouac for editorial handling.

REFERENCES

Abdurachman, E.K., Bourdier, J.-L., Voight, B., 2000. Nuées ardentes of 22 November 1994 at Merapi volcano, Java, Indonesia. Journal of Volcanology and Geothermal Research 100, 345–361. https://doi.org/10.1016/S0377-0273(00)00144-X

Bagnardi, M., González, P.J., Hooper, A., 2016. High-resolution digital elevation model from tri-stereo Pleiades-1 satellite imagery for lava flow volume estimates at Fogo Volcano. Geophysical Research Letters 43, 6267–6275. https://doi.org/10.1002/2016GL069457

Betancourt, M.J., Girolami, M., 2013. Hamiltonian Monte Carlo for Hierarchical Models. arXiv:1312.0906 [stat].

Burns, J.H.R., Delparte, D., Gates, R.D., Takabayashi, M., 2015. Integrating structure-from-motion photogrammetry with geospatial software as a novel technique for quantifying 3D ecological characteristics of coral reefs. PeerJ 3, e1077. https://doi.org/10.7717/peerj.1077

Carpenter, B., Gelman, A., Hoffman, M.D., Lee, D., Goodrich, B., Betancourt, M., Brubaker, M., Guo, J., Li, P., Riddell, A., 2017. Stan: A Probabilistic Programming Language.

649 Journal of Statistical Software; Vol 1, Issue 1 (2017).
650 https://doi.org/10.18637/jss.v076.i01
651 Carrara, A., Pinel, V., Bascou, P., Chaljub, E., De la Cruz-Reyna, S., 2019. Post-emplacement
652 dynamics of andesitic lava flows at Volcán de Colima, Mexico, revealed by radar and
653 optical remote sensing data. Journal of Volcanology and Geothermal Research 381, 1–
654 15. https://doi.org/10.1016/j.jvolgeores.2019.05.019
655 Cassidy, M., Manga, M., Cashman, K., Bachmann, O., 2018. Controls on explosive-effusive
656 volcanic eruption styles. Nature Communications 9, 2839.
657 https://doi.org/10.1038/s41467-018-05293-3
658 Cole, P.D., Calder E. S., Druitt T. H., Hoblitt R., Robertson R., Sparks R. S. J., Young S. R.,
659 1998. Pyroclastic flows generated by gravitational instability of the 1996–97 Lava
660 Dome of Soufriere Hills Volcano, Montserrat. Geophysical Research Letters 25,
661 3425–3428. https://doi.org/10.1029/98GL01510
662 Coppola, D., Laiolo, M., Lara, L.E., Cigolini, C., Orozco, G., 2016. The 2008 "silent"
663 eruption of Nevados de Chillán (Chile) detected from space: Effusive rates and trends
664 from the MIROVA system. Journal of Volcanology and Geothermal Research 327,
665 322–329. https://doi.org/10.1016/j.jvolgeores.2016.08.016
666 Di Traglia, F., Calvari, S., D'Auria, L., Nolesini, T., Bonaccorso, A., Fornaciai, A., Esposito,
667 A., Cristaldi, A., Favalli, M., Casagli, N., 2018. The 2014 Effusive Eruption at
668 Stromboli: New Insights from In Situ and Remote-Sensing Measurements. Remote
669 Sensing 10, 2035. https://doi.org/10.3390/rs10122035
670 Diefenbach, A.K., Bull, K.F., Wessels, R.L., McGimsey, R.G., 2013. Photogrammetric
671 monitoring of lava dome growth during the 2009 eruption of Redoubt Volcano.
672 Journal of Volcanology and Geothermal Research, The 2009 Eruption of Redoubt
673 Volcano, Alaska 259, 308–316. https://doi.org/10.1016/j.jvolgeores.2011.12.009

674 Dingwell, D.B., 1996. Volcanic Dilemma: Flow or Blow? Science 273, 1054–1055.
675 Dixon, H.J., Murphy, M.D., Sparks, S.J., Chávez, R., Naranjo, J.A., Dunkley, P.N., Young,
676 S.R., Gilbert, J.S., Pringle, M.R., 1999. The geology of Nevados de Chillán volcano,
677 Chile. Revista geológica de Chile 26, 227–253. https://doi.org/10.4067/S0716-
678 02081999000200006
679 Eichelberger, J.C., Carrigan, C.R., Westrich, H.R., Price, R.H., 1986. Non-explosive silicic
680 volcanism. Nature 323, 598–602. https://doi.org/10.1038/323598a0
681 Farr, T.G., Rosen Paul A., Caro Edward, Crippen Robert, Duren Riley, Hensley Scott,
682 Kobrick Michael, Paller Mimi, Rodriguez Ernesto, Roth Ladislav, Seal David, Shaffer
683 Scott, Shimada Joanne, Umland Jeffrey, Werner Marian, Oskin Michael, Burbank
684 Douglas, Alsdorf Douglas, 2007. The Shuttle Radar Topography Mission. Reviews of
685 Geophysics 45. https://doi.org/10.1029/2005RG000183
686 Fink, J.H., 1987. The Emplacement of Silicic Domes and Lava Flows. Geological Society of
687 America.
688 Fink, J.H., Malin, M.C., Anderson, S.W., 1990. Intrusive and extrusive growth of the Mount
689 St Helens lava dome. Nature 348, 435–437. https://doi.org/10.1038/348435a0
690 Ganci, G., Cappello, A., Bilotta, G., Corradino, C., Del Negro, C., 2019a. Satellite-Based
691 Reconstruction of the Volcanic Deposits during the December 2015 Etna Eruption.
692 Data 4, 120. https://doi.org/10.3390/data4030120
693 Ganci, G., Cappello, A., Zago, V., Bilotta, G., Herault, A., Negro, C.D., 2019b. 3D Lava flow
694 mapping of the 17–25 May 2016 Etna eruption using tri-stereo optical satellite data.
695 Annals of Geophysics 62, 220. https://doi.org/10.4401/ag-7875
696 Gleyzes, M.A., Perret, L., Kubik, P., 2012. Pleiades System Architecture and Main
697 Performances. ISPRS - International Archives of the Photogrammetry, Remote

698 Sensing and Spatial Information Sciences 39B1, 537.
699 https://doi.org/10.5194/isprsarchives-XXXIX-B1-537-2012
700 Gorshkov, G.S., 1959. Gigantic eruption of the volcano bezymianny. Bull Volcanol 20, 77–
701 109. https://doi.org/10.1007/BF02596572
702 Görtler, J., Kehlbeck, R., Deussen, O., 2019. A Visual Exploration of Gaussian Processes.
703 Distill 4, e17.
704 Gueugneau, V., Kelfoun, K., Druitt, T., 2019. Investigation of surge-derived pyroclastic flow
705 formation by numerical modelling of the 25 June 1997 dome collapse at Soufrière
706 Hills Volcano, Montserrat. Bull Volcanol 81, 25. https://doi.org/10.1007/s00445-019-
707 1284-y
708 Harris, A.J.L., Dehn, J., Calvari, S., 2007. Lava effusion rate definition and measurement: a
709 review. Bull Volcanol 70, 1. https://doi.org/10.1007/s00445-007-0120-y
710 Jaupart, C., Allègre, C.J., 1991. Gas content, eruption rate and instabilities of eruption regime
711 in silicic volcanoes. Earth and Planetary Science Letters 102, 413–429.
712 https://doi.org/10.1016/0012-821X(91)90032-D
713 Kaneko, T., Wooster, M.J., Nakada, S., 2002. Exogenous and endogenous growth of the
714 Unzen lava dome examined by satellite infrared image analysis. Journal of
715 Volcanology and Geothermal Research 116, 151–160. https://doi.org/10.1016/S0377-
716 0273(02)00216-0
717 Kelfoun, K., 2017. A two-layer depth-averaged model for both the dilute and the concentrated
718 parts of pyroclastic currents. Journal of Geophysical Research: Solid Earth 122, 4293–
719 4311. https://doi.org/10.1002/2017JB014013
720 Kelfoun, K., Gueugneau Valentin, Komorowski Jean-Christophe, Aisyah Nurnaning, Cholik
721 Noer, Merciecca Charley, 2017. Simulation of block-and-ash flows and ash-cloud
722 surges of the 2010 eruption of Merapi volcano with a two-layer model. Journal of

723 Geophysical Research: Solid Earth 122, 4277–4292.
724 https://doi.org/10.1002/2017JB013981
725 Komorowski, J.-C., Jenkins, S., Baxter, P.J., Picquout, A., Lavigne, F., Charbonnier, S.,
726 Gertisser, R., Preece, K., Cholik, N., Budi-Santoso, A., Surono, 2013. Paroxysmal
727 dome explosion during the Merapi 2010 eruption: Processes and facies relationships of
728 associated high-energy pyroclastic density currents. Journal of Volcanology and
729 Geothermal Research, Merapi eruption 261, 260–294.
730 https://doi.org/10.1016/j.jvolgeores.2013.01.007
731 Lipman, P., Mullineaux, D., 1981. The 1980 eruptions of Mount St. Helens, Washington. U.S.
732 Dept. of the Interior, U.S. Geological Survey, Washington.
733 Lowe, D.G., 2004. Distinctive Image Features from Scale-Invariant Keypoints. International
734 Journal of Computer Vision 60, 91–110.
735 https://doi.org/10.1023/B:VISI.0000029664.99615.94
736 Martel, C., Iacono-Marziano, G., 2015. Timescales of bubble coalescence, outgassing, and
737 foam collapse in decompressed rhyolitic melts. Earth and Planetary Science Letters
738 412, 173–185. https://doi.org/10.1016/j.epsl.2014.12.010
739 Mendoza-Rosas, A.T., Gómez-Vázquez, Á., De la Cruz-Reyna, S., 2017. Statistical analysis
740 of the sustained lava dome emplacement and destruction processes at Popocatépetl
741 volcano, Central México. Bull Volcanol 79, 43. https://doi.org/10.1007/s00445-017-
742 1127-7
743 Miller, T.P., 1994. Dome growth and destruction during the 1989–1990 eruption of redoubt
744 volcano. Journal of Volcanology and Geothermal Research, The 1989-1990 Eruptions
745 of Redoubt Volcano, Alaska 62, 197–212. https://doi.org/10.1016/0377-
746 0273(94)90034-5

747 Moussallam, Y., Bani, P., Schipper, C.I., Cardona, C., Franco, L., Barnie, T., Amigo, Á.,
748 Curtis, A., Peters, N., Aiuppa, A., Giudice, G., Oppenheimer, C., 2018. Unrest at the
749 Nevados de Chillán volcanic complex: a failed or yet to unfold magmatic eruption? 1
750 1, 19–32. https://doi.org/10.30909/vol.01.01.1932
751 Moussallam, Y., Rose-Koga, E.F., Koga, K.T., Médard, E., Bani, P., Devidal, J.-L., Tari, D.,
752 2019. Fast ascent rate during the 2017–2018 Plinian eruption of Ambae (Aoba)
753 volcano: a petrological investigation. Contrib Mineral Petrol 174, 90.
754 https://doi.org/10.1007/s00410-019-1625-z
755 Nakada, S., Miyake, Y., Sato, H., Oshima, O., Fujinawa, A., 1995. Endogenous growth of
756 dacite dome at Unzen volcano (Japan), 1993–1994. Geology 23, 157–160.
757 https://doi.org/10.1130/0091-7613(1995)023<0157:EGODDA>2.3.CO;2
758 Naranjo, J.A., Chavez, R., Sparks, R.S.J., Gilbert, J., Dunkley, P.N., 1994. Nuevos
759 antecedentes sobre la evolución Cuaternaria del Complejo Volcánico Nevados de
760 Chillán, in: Congreso Geológico Chileno, 7. Concepción, pp. 342–345.
761 Newhall, C.G., Melson, W.G., 1983. Explosive activity associated with the growth of
762 volcanic domes. Journal of Volcanology and Geothermal Research, Explosive
763 Volcanism 17, 111–131. https://doi.org/10.1016/0377-0273(83)90064-1
764 Newhall, C.G., Pallister, J.S., 2015. Chapter 8 - Using Multiple Data Sets to Populate
765 Probabilistic Volcanic Event Trees, in: Shroder, J.F., Papale, P. (Eds.), Volcanic
766 Hazards, Risks and Disasters. Elsevier, Boston, pp. 203–232.
767 https://doi.org/10.1016/B978-0-12-396453-3.00008-3
768 Nguyen, C.T., Gonnermann, H.M., Houghton, B.F., 2014. Explosive to effusive transition
769 during the largest volcanic eruption of the 20th century (Novarupta 1912, Alaska).
770 Geology 42, 703–706. https://doi.org/10.1130/G35593.1

771 Ogburn, S.E., Calder, E.S., 2012. DomeHaz: Dome-forming eruptions database. On Vhub at
772 https://vhub.org/groups/domedatabase.
773 Ogburn, S.E., Loughlin, S.C., Calder, E.S., 2015. The association of lava dome growth with
774 major explosive activity (VEI ≥ 4): DomeHaz, a global dataset. Bull Volcanol 77, 40.
775 https://doi.org/10.1007/s00445-015-0919-x
776 Papaspiliopoulos, O., Roberts, G.O., Sköld, M., 2007. A General Framework for the
777 Parametrization of Hierarchical Models. Statist. Sci. 22, 59–73.
778 https://doi.org/10.1214/088342307000000014
779 Patrick, M.R., Dietterich, H.R., Lyons, J.J., Diefenbach, A.K., Parcheta, C., Anderson, K.R.,
780 Namiki, A., Sumita, I., Shiro, B., Kauahikaua, J.P., 2019. Cyclic lava effusion during
781 the 2018 eruption of Kīlauea Volcano. Science 366.
782 https://doi.org/10.1126/science.aay9070
783 Pierrot-Deseilligny, M., Jouin, D., Belvaux, J., Maillet, G., Girod, L., Rupnik, E., Muller, J.,
784 Daakir, M., Choqueux, G., Deveau, M., 2014. Micmac, apero, pastis and other
785 beverages in a nutshell. Institut Géographique National.
786 Riihimäki, J., Vehtari, A., 2010. Gaussian processes with monotonicity information, in:
787 Proceedings of the Thirteenth International Conference on Artificial Intelligence and
788 Statistics. Presented at the Proceedings of the Thirteenth International Conference on
789 Artificial Intelligence and Statistics, pp. 645–652.
790 Rupnik, E., Daakir, M., Pierrot Deseilligny, M., 2017. MicMac – a free, open-source solution
791 for photogrammetry. Open Geospatial Data, Software and Standards 2, 14.
792 https://doi.org/10.1186/s40965-017-0027-2
793 Sato, H., Fujii, T., Nakada, S., 1992. Crumbling of dacite dome lava and generation of
794 pyroclastic flows at Unzen volcano. Nature 360, 664–666.
795 https://doi.org/10.1038/360664a0

796 Saucedo, R., Macías, J.L., Bursik, M.I., Mora, J.C., Gavilanes, J.C., Cortes, A., 2002.
797 Emplacement of pyroclastic flows during the 1998–1999 eruption of Volcán de
798 Colima, México. Journal of Volcanology and Geothermal Research 117, 129–153.
799 https://doi.org/10.1016/S0377-0273(02)00241-X
800 Schilling, S.P., Thompson, R.A., Messerich, J.A., Iwatsubo, E.Y., 2008. Use of digital
801 aerophotogrammetry to determine rates of lava dome growth, Mount St. Helens,
802 Washington, 2004-2005: Chapter 8 in A volcano rekindled: the renewed eruption of
803 Mount St. Helens, 2004-2006 (USGS Numbered Series No. 1750–8), Professional
804 Paper. U.S. Geological Survey, Reston, VA.
805 Shea, T., 2017. Bubble nucleation in magmas: A dominantly heterogeneous process? Journal
806 of Volcanology and Geothermal Research 343, 155–170.
807 https://doi.org/10.1016/j.jvolgeores.2017.06.025
808 Shean, D.E., Alexandrov, O., Moratto, Z.M., Smith, B.E., Joughin, I.R., Porter, C., Morin, P.,
809 2016. An automated, open-source pipeline for mass production of digital elevation
810 models (DEMs) from very-high-resolution commercial stereo satellite imagery. ISPRS
811 Journal of Photogrammetry and Remote Sensing 116, 101–117.
812 https://doi.org/10.1016/j.isprsjprs.2016.03.012
813 Swanson, D.A., Holcomb, R.T., 1990. Regularities in Growth of the Mount St. Helens Dacite
814 Dome, 1980–1986, in: Lava Flows and Domes, IAVCEI Proceedings in Volcanology.
815 Springer, Berlin, Heidelberg, pp. 3–24. https://doi.org/10.1007/978-3-642-74379-5_1
816 Wolpert, R.L., Ogburn, S.E., Calder, E.S., 2016. The longevity of lava dome eruptions.
817 Journal of Geophysical Research: Solid Earth 121, 676–686.
818 https://doi.org/10.1002/2015JB012435
819 Woods, A.W., Koyaguchi, T., 1994. Transitions between explosive and effusive eruptions of
820 silicic magmas. Nature 370, 641–644. https://doi.org/10.1038/370641a0

821 Woods, A.W., Sparks, R.S.J., Ritchie, L.J., Batey, J., Gladstone, C., Bursik, M.I., 2002. The
822 explosive decompression of a pressurized volcanic dome: the 26 December 1997
823 collapse and explosion of Soufrière Hills Volcano, Montserrat. Geological Society,
824 London, Memoirs 21, 457–465. https://doi.org/10.1144/GSL.MEM.2002.021.01.20
825 Yokoyama, I., 2005. Growth rates of lava domes with respect to viscosity of magmas. Annals
826 of Geophysics 48. https://doi.org/10.4401/ag-3246
827